Phenotypic size heterogeneity is a viral mechanism of persistence

Tian Li[1], Zhenyu Li[1], Meisui Liu[1], Erin E. Deans[1], Tijana Ivanovic[1*]

[1] Biochemistry Department, Brandeis University, Waltham, MA, USA

[*] Correspondence: ivanovic@brandeis.edu

ABSTRACT

Many enveloped animal viruses, including emerging human pathogens Ebola, Nipah, and Hendra viruses, produce a mixture of virus-particle sizes including very long, filamentous members[1-4]. However, the function of the filamentous particles is unknown. The main impediments to characterizing viral filaments are their phenotypic origin (a single infecting particle gives rise to a range of particle sizes)[5,6], difficulty of purifying particles to homogeneity according to their size, and the apparent lack of filament advantage *in vitro*[7,8]. Influenza virus particles range in length by three orders of magnitude (~55 nm to ~30 µm). All influenza particles package at most a single genome, but the total number of the surface-exposed viral glycoproteins, hemagglutinin (HA) and neuraminidase (NA), and the HA/NA ratio scale with particle length[6,9,10]. HA is the cell-entry protein of influenza, which mediates fusion between the viral and the endosomal membranes by the combined action of 3-5 active HA neighbors (fusion cluster)[11-13]. Here we identify influenza filaments as viral persisters increasing the probability of fusion-cluster formation and cell entry under HA-directed selective pressure. We fractionated viruses to enrich for spherical or filamentous particles and measured the single-particle kinetics of membrane fusion. As a surrogate for HA-directed selective pressure, we used a Fab fragment of a broadly neutralizing antibody that inactivates bound HA[14]. In its presence, filamentous particles fuse more rapidly and more efficiently than do spherical ones. We show that the infectious advantage of filaments derives from their enhanced fusion efficiency rather than from rate effects. Filaments also offer universal protection from extreme HA inactivation. Our results show how the virus can adapt to any condition limiting HA function, and suggest targeting viral filaments as a strategy to prolong vaccine effectiveness or to thwart viral pandemic adaptation.

INTRODUCTION

Viruses present tractable systems with which to dissect universal mechanisms. The phenomenon of phenotypic diversity that benefits a population under changing pressure is known even among higher organisms[15], and is best studied in bacteria, where the role of bacterial persistence in antibiotic resistance is well documented[16,17]. Persisters are defined as a small subpopulation of bacteria that survive antibiotic treatment, but after antibiotic removal, expand into a population with the same antibiotic sensitivity as the original population. Under sustained pressure, persisters give rise to (genetic) resistance. The molecular players that generate diversity are in some cases starting to emerge[17]. However, defining the underlying mechanisms that confer benefit under a given set of conditions is challenging because of the small numbers and phenotypic origin of the beneficial members. The relative simplicity of viral structure might offer a tractable system with which to probe functional differences among members.

Influenza filaments are advantageous and persist *in vivo*, but are quickly replaced by spherical particles during virus passaging *in vitro*[18,19]. Spherical particles are taken up by cells via clathrin-mediated endocytosis, and filaments via a slower and more energy-requiring macropinocytosis[20]. Furthermore, the assembly of filaments takes up tremendous resources (e.g. membranes and viral proteins), but they package the same, single-genome cargo[9,10,21]. It is thus assumed that to understand the benefit of viral filaments, a full complexity of *in-vivo* infections needs to be considered. However, the relative simplicity of virus structure offers hints into the filament function. Influenza virus has three structural proteins whose numbers scale with particle size: the matrix protein, M1, which forms the particle shape, and the surface-exposed HA and NA[9,10]. HA densely covers at least 80% of the viral surface and its relative representation is higher on longer particles at the expense of NA[6,9,10]. HA is the main target of neutralizing antibodies and is thus under constant pressure to evolve[22]. Furthermore, adaptation of HA to human-cell entry is a key determinant of influenza pandemics, so viral zoonotic transmission is another source of selective pressure on HA[23]. Presentation of HA on particles of different sizes might offer an adaptability benefit, and detailed dissection of HA function in different particle contexts should reveal its mechanism.

HA is synthesized as an inactive trimer, HA0[24]. Activation requires cleavage of each HA0 monomer into two disulfide-linked subunits, HA1 and HA2[25]. For cell entry, HA1 engages the sialic-acid receptor on the target-cell surface, and HA2 mediates membrane fusion in the late endosome. Individual HA1-sialic acid interactions are weak (2-3 mM K_d), but multivalent virus binding results in femtomolar avidities[26]. The contact interface (patch) between the virus particle and the membrane incorporates ~50 HAs for the spherical particles, and this number scales approximately linearly with particle length[9-11] (Fig. 1a). Membrane fusion results from a functional interplay among HAs within the contact patch. Cleaved HA is metastable; low pH reduces the barrier for transition to the stable postfusion conformation[27]. Initial HA triggering is stochastic, but inducing membrane merger requires the combined free energy released by the HA conformational changes of 3-5 neighboring trimers[11,12]. A hydrophobic peptide sequence at the N-terminus of HA2, termed the fusion peptide (FP), mediates functional coupling of HA conformational changes to membrane fusion. In the pre-fusion HA, FP inserts in a conserved

cavity (the pre-fusion pocket) at the base of HA near the viral membrane[24]. During HA conformational changes in the contact patch, FP either inserts in the target membrane (productive HA), or, if HA assumes the post-fusion state without engaging the target membrane, FP inserts back into the viral membrane (unproductive HA)[12,28]. The release of FP from the pre-fusion pocket is the rate-limiting structural rearrangement influencing the rate of fusion-cluster formation[11]. The frequency of unproductive HAs, which imposes restrictions on the available geometries for adjacent HA insertions, influences the rate and probability of fusion-cluster formation[12,29]. While membrane resistance prevents individual inserted HAs from folding back, the fold-back for HAs in the fusion cluster is cooperative and fast[11].

Prediction from stochastic simulations

The larger patch size afforded by viral filaments should increase the total number of inserted HAs and thus the efficiency and/or rate of membrane fusion under any condition limiting HA activity, e.g. large fraction of unproductive HA, low level of HA0 activation, or HA inactivation by antibodies or inhibitors (Fig. 1a). To express these predictions in quantitative terms, we performed stochastic simulations of fusion for a 600-fold range of patch sizes and zero to 80-97% HA inactivation (Fig. 1b). The probability of fusion-cluster formation for spherical particles declines for HA inactivation greater than 20% (PS 55), but a 600-times larger patch requires at

Figure 1

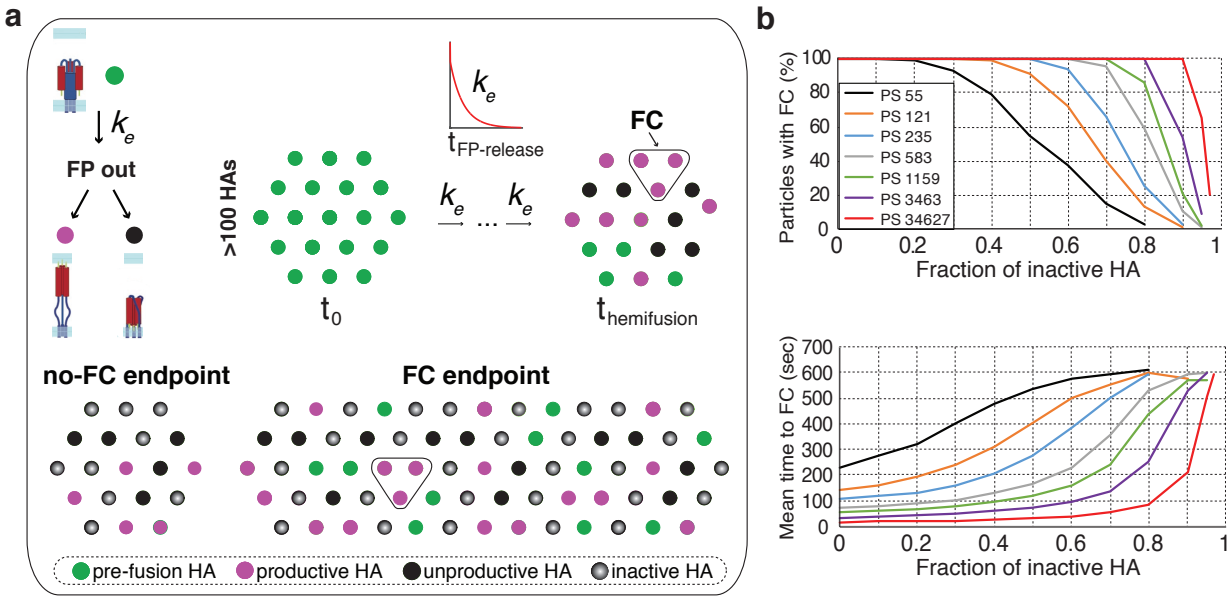

Figure 1 | Stochastic simulations. a, Stochastic fusion model[12]. A simplified contact patch before fusion (t_0) or at the time of fusion-cluster (FC) formation ($t_{hemifusion}$) is shown (*top*). Random HAs extend and insert into the target membrane (green – pre-fusion HA; magenta – inserted HA) or become inactivated (black – unproductive HA). k_e is the rate of FP release. Under the same limiting condition, longer particles have a higher probability of fusion-cluster formation (*bottom*). The prediction is illustrated with an elliptical patch, but the simulations used circular patches (see Methods). **b**, Simulation results for the yield and mean lag-time to fusion-cluster formation at 0.02-0.1 inactive HA-fraction increments from datasets with at least 1000 fusion clusters. PS, patch size.

least 90% HA inactivation for the same effect, and yields 20% fusion for 97% inactive HAs (PS 34627). Larger patches form fusion clusters more rapidly, but rate differences get smaller for more HA inactivation. Overall, larger patch size enables higher efficiency and/or rate of fusion-cluster formation depending on the extent of HA inactivation.

Functional advantage of filaments

To compare the predictions from stochastic simulations with experiment, we used filamentous influenza virus, X31HA/Udorn, in single-particle experiments of membrane fusion[11]. Analysis of individual particles can reveal subpopulations with distinct kinetics, and in this way obviate the need for homogeneous particle preparations. We devised a strategy for particle size-enrichment using cycles of centrifugation at low relative centrifugal force, which preferentially sediments filamentous particles. We analyzed the resultant fractions by negative-stain electron microscopy (Fig. 2a-b, Tables 1 and 2). The supernatant fraction (SUP) has a relatively narrow and symmetric particle-size distribution, with 95% of the population ranging in length from 50 nm to 250 nm. Taking 250 nm as the cut off, the pellet fraction (PELLET) includes 47.2% filaments, whose average length is ~5-times that of the SUP particles (Table 1).

To produce a variable, measurable limit to HA activity, we used a Fab fragment of a broadly neutralizing antibody, MEDI8852 (M-Fab), which binds the base of HA and prevents HA conformational changes[14]. Fluorescently tagged M-Fab binding to unlabeled particles shows a narrow distribution of particle intensities for the SUP particles, and a wider fluorescence-intensity distribution with a long tail for the PELLET particles (Fig. 2c). M-Fab binding thus scales with particle length. Incubation of M-Fab-bound particles at low pH did not significantly change fluorescence-intensity distributions (Fig. 2c), validating M-Fab as a reagent that inactivates targeted HA for at least the duration of these experiments, an assumption of stochastic simulations (Fig. 1).

We performed membrane fusion experiments with DiD-labeled SUP or PELLET particles on supported planar membrane bilayers for a range of unlabeled M-Fab concentrations at pH5.2 (Supplemental Videos 1-4). We extracted individual-particle lag times from pH drop to hemifusion (onset of DiD dequenching), a fusion intermediate that reports on fusion-cluster formation and invariably precedes pore opening[11,30]. We fitted frequency distributions of hemifusion lag times with gamma probability density and derived mean lag times from the fits[12,30] (Fig. 3a). The plots of hemifusion yield and time for a range of M-Fab concentrations both show that the PELLET particles are less sensitive to HA inactivation than the SUP particles (Fig. 3b). We derived hemifusion yield and lag-time distributions for the long (>250 nm) particles within the PELLET as described in the Methods (Fig. 3c). The resultant plots of SUP versus long particles match the prediction from stochastic simulations for patch-size pairs where the larger patch size is ~4-5 times the size of the smaller one (e.g. 55/235 or 121/583) (Fig. 1b); the derived patch-size ratio in turn agrees with the measured ratio of the filament and SUP-particle average lengths (Table 1). The combined results thus validate the stochastic fusion model[12], and support our hypothesis that the larger patch size afforded by viral filaments increases the rate and probability of fusion-cluster formation under limiting HA activity.

Figure 2

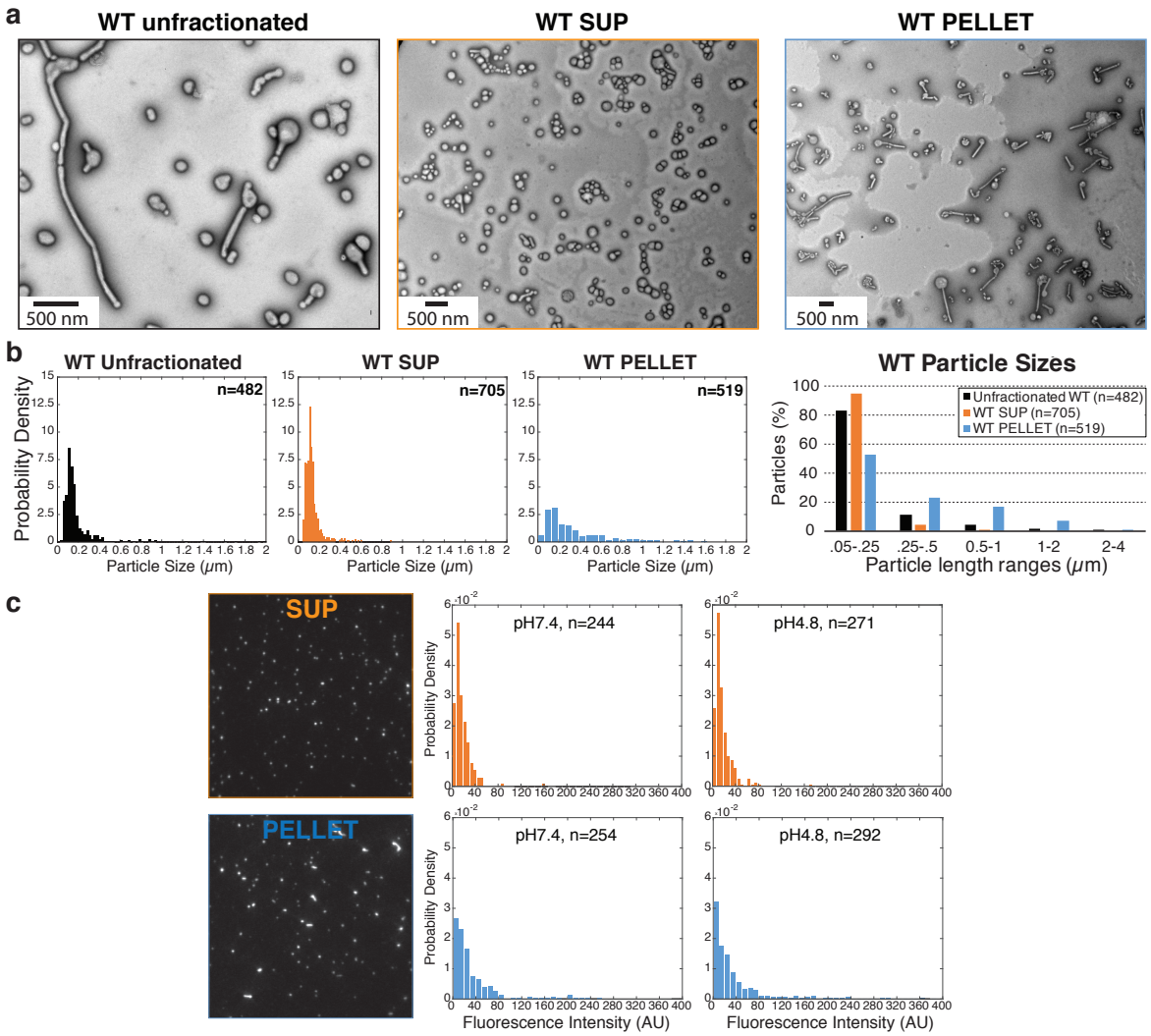

Figure 2 | Particle fractionation. a, Representative negative-stain electron micrographs of WT particle fractions. **b**, Particle-length measurements of WT fractions. **c**, Quantification of fluorescent M-Fab binding to unlabeled WT particles. Glass coverslips were passivated with a mixture of polyethylene glycol (PEG) and PEG-biotin. Biotinylated antibody targeting HA1 is specifically captured with neutravidin, and it recruits virus particles. Virus particles were pre-incubated with 134 nM JF-549-tagged M-Fab before capture, and unbound M-Fab was washed away after capture. Representative particle-images (*left*), and particle fluorescence-intensity quantification at neutral pH (*middle*), or after 20 minutes at pH 4.8 (*right*).

		Overall mean (nm)	Overall median (nm)	Filaments mean (nm)	Filaments median (nm)	% Filaments	# particles
WT	unfractionated	211.5	136.0	616.1	385.7	17.0	482
	SUP	132.7	117.4	391.6	343.8	5.1	705
	PELLET	380.9	233.5	647.7	514.0	47.2	519
D112A	SUP	143.8	129.5	328.7	294.2	6.3	552
	PELLET	420.7	210.0	786.0	524.3	42.9	457
H17Y	SUP	136.5	128.7	342.3	275.9	3.83	470
	PELLET	289.0	191.3	554.3	419.5	34.0	770

Table 1 (*above*) | WT particle lengths, and percent long particles in fractions.

	>50 nm	>250 nm	>500 nm	>750 nm	>1000 nm
SUP	99.8	5.1	0.9	0.14	0
PELLET	99.6	47.2	24.3	13.1	7.71
%PELLET/%SUP	1.0	9.3	28.6	93.6	N/A

Table 2 (*above*) | Percent of WT particles longer than the specified lengths.

Figure 3

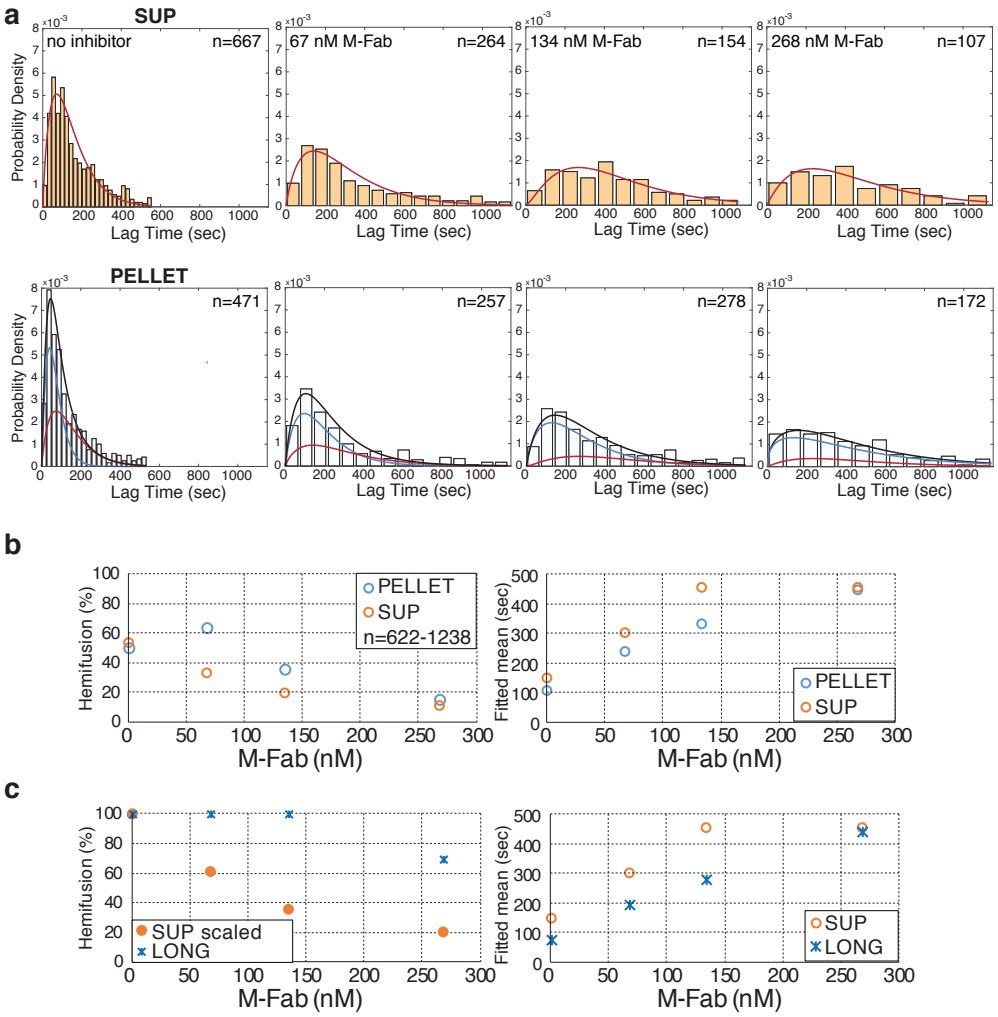

Figure 3 | Single-particle membrane fusion of short and long particles. a, Hemifusion lag times with gamma-distribution fit (SUP, red line), or bi-gamma fit (PELLET, black line) with the underlying distributions for the short (red line) and long (blue line) PELLET-particle subpopulations. Data were pooled from several experiments where each condition was represented on each day. **b**, Hemifusion yield, and fitted mean from panel **a**. **c**, Derived hemifusion yield and fitted mean for long particles in PELLET.

Increased infectivity of filaments

To determine whether viral filaments offer infectivity advantage under HA-directed selective pressures, we measured the SUP- and PELLET-particle concentrations (in hemagglutination units per ml; HAU/ml) needed to induce 50% cell death for a range of M-Fab concentrations in a single-cycle of infection ($scTCID_{50}$) (Fig. 4). We limited infections to a single cycle because particle-size separation is possible only for the initial infection, which then yields pleomorphic progeny[5,6]. In the absence of inhibition, the PELLET has no infectivity advantage (and in some experiments a subtle disadvantage) over the SUP (Fig. 4a), consistent with previous reports for viral filaments[7,8]. However, the effect of M-Fab on the $scTCID_{50}$ of the PELLET is lower than its effect on the SUP, with the PELLET advantage ranging from 50% (17 nM M-Fab) to greater than 3-fold (268 nM M-Fab) (Fig. 4b). The $scTCID_{50}$ data confirm that influenza virus sensitivity to HA inhibition decreases with increase in virus-particle length.

Figure 4

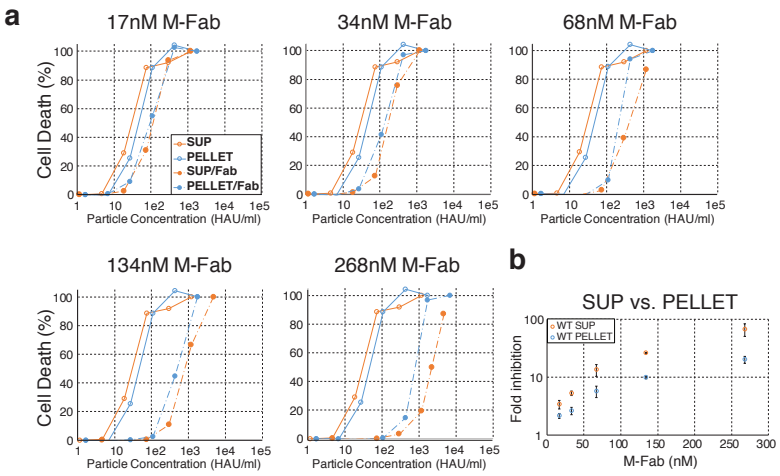

Figure 4 | Filament infectivity advantage under HA inhibition. **a**, A representative set of $scTCID_{50}$ measurements at various M-Fab concentrations. The no-inhibitor baseline for PELLET and SUP from which infectivity shifts are measured is shown on all plots. **b**, Fold increase in $scTCID_{50}$ for M-Fab-treated samples. Average and standard deviation of three independent experiments are shown.

Effect of HA inactivation on infectivity

The protective effect of filaments for a given level of HA inactivation could stem from their increase in the fusion rate, yield, or both (Fig. 3c). To test whether kinetics of fusion-cluster formation influences infectivity outcomes, we employed virus mutants with (de)stabilized pre-fusion HA. A mutation in HA2, $D112_2A$, destabilizes FP in its pre-fusion pocket resulting in faster hemifusion[11]. A mutation in HA1, $H17_1Y$, stabilizes FP in its pre-fusion pocket and is predicted to slow hemifusion[31]. The extent of fluorescent M-Fab binding to WT and $D112_2A$ particles is the same, and to $H17_1Y$ only slightly reduced, implying the same or very similar extent of HA inactivation for a given M-Fab concentration (Fig. 5a). Indeed, single-particle measurements for WT and $D112_2A$ give very similar hemifusion-yield curves, and a similar relative change in hemifusion lag-times (Fig. 5b). However, $D112_2A$ particles are 7 to 11 times faster in hemifusion for the tested range of M-Fab concentrations, owing to the faster rate of fusion-peptide release for the mutant[11]. At even the highest M-Fab concentration, hemifusion of $D112_2A$ particles is 2.4-fold faster than that of the uninhibited WT. $H17_1Y$, on the other hand, is so stabilized that it has lower hemifusion yield at pH 5.2, either because of a lower extent of HA activation or lower productiveness (Fig. 5c). At pH 4.8, hemifusion yield of $H17_1Y$ is comparable to WT, but hemifusion rate is markedly lower for the mutant. Unlike the large changes in the rate of hemifusion for HA mutations, even the highest concentration of M-Fab tested slows hemifusion of the short particles less than 5-fold (Fig. 3b, 5b-c). Thus, the HA mutants allow us to probe the effects of altered hemifusion-rates on infectivity.

We compared WT, $D112_2A$, and $H17_1Y$ viruses in $scTCID_{50}$ experiments (Fig. 5d-f). The baseline titers of $D112_2A$ and $H17_1Y$ viruses are within 2-3-fold of WT, showing that cell entry is relatively insensitive to the rate of fusion-cluster formation (Fig. 5d). Furthermore, WT and $D112_2A$ viruses are equally sensitive to all tested M-Fab concentrations, confirming that the rate increase afforded by HA destabilization does not boost infectivity under HA pressure (Fig. 5e). $H17_1Y$ is more sensitive to HA inactivation than WT and $D112_2A$ viruses, but otherwise follows the same trend for the higher M-Fab concentration (Fig. 5e). The higher sensitivity of $H17_1Y$ to M-Fab can be interpreted in the context of this mutant's lower hemifusion yield at the pH of

endosomes (Fig. 5c, pH 5.2). If the lower rate of fusion-cluster formation for $H17_1Y$ contributed to its higher sensitivity to M-Fab, a further increase in M-Fab concentration would inhibit $H17_1Y$ disproportionately, causing it deviate from the WT/$D112_2A$ infectivity curves. The same infectivity trend for $H17_1Y$ confirms that cell entry of even the slow-fusing $H17_1Y$ mutant is insensitive to rate changes caused by HA inactivation (Fig. 5e). M-Fab thus lowers infectivity by lowering the number of particles that successfully assemble fusion clusters.

Figure 5

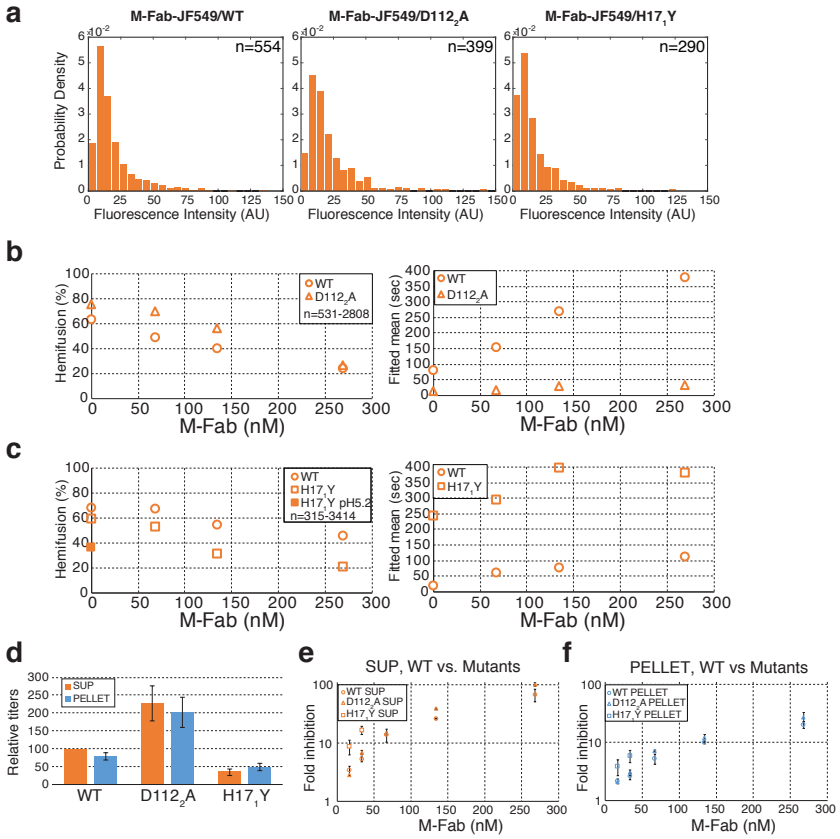

Figure 5 | HA inhibition reduces the number of particles assembling fusion clusters. a, Quantification of fluorescent M-Fab binding to unlabeled particles. Particle fluorescence-intensity quantification after 20 minutes at pH 4.8. **b-c**, Single-particle hemifusion yield and fitted mean for a range of M-Fab concentrations for short particles, $D112_2A$ at pH 5.2 (**b**) and $H17_1Y$ at pH 4.8 (*open symbols*) or pH 5.2 (*closed symbol*) (**c**). **d**, Baseline $scTCID_{50}$ titers normalized to WT SUP. Average and standard deviation of three independent experiments are shown. **e-f**, Fold increase in $scTCID_{50}$ for M-Fab-treated samples relative to untreated samples for SUP (**e**) or PELLET (**f**). Average and standard deviation of three independent experiments are shown. WT data is replotted from Fig. 4b for direct comparison.

Filaments resist extreme HA inactivation

The unproductive HA fraction contributes to the overall probability of virus particles assembling fusion clusters and determines how sensitive particles will be to HA inactivation (Fig. 1a)[12,29]. The effect of M-Fab on fusion-cluster formation in endosomes (Fig. 5e) is much greater than its effect *in vitro* (Fig. 5b-c). For example, 67 nM of M-Fab reduces $scTCID_{50}$ titers 14-fold for the WT and $D112_2A$ SUP particles, but hemifusion-yield changes are comparably small for this M-Fab concentration *in vitro*. Productive HAs are thus less frequent in endosomes than on planar membrane bilayers, and inactivation of a small subset of HAs prevents a majority of virus particles in endosomes from assembling fusion clusters.

The effect of M-Fab on the $scTCID_{50}$ of $D112_2A$ or $H17_1Y$ PELLET is lower than its effect on the corresponding SUP, with PELLET advantage being the same for the mutants as for the WT (Fig. 5e-f). We interpret PELLET advantage as resulting from more opportunities for fusion-

cluster formation on longer particles (Fig. 1a). This interpretation predicts that infectivity differences between PELLET and SUP fractions would be greater for HA-inactivation levels that affect very long filaments because PELLET and SUP particle distributions are more different for longer particles (Table 2). To test this prediction, we prepared virus particles with less than 1% activating HA0 cleavage (Fig. 6a). We then measured the loss of infectivity for the uncleaved virus, or the uncleaved virus pre-treated with M-Fab, relative to fully cleaved, untreated virus in a modified plaque-assay experiment (Fig. 6b). The result for the control (cleaved, M-Fab pre-treated) virus matched the $scTCID_{50}$ data at this M-Fab concentration (Fig. 4) with the PELLET offering approximately 3-fold higher infectivity than the SUP (Fig. 6b). A similar result was obtained for the uncleaved virus. Consistent with our prediction for extreme HA pressure, the uncleaved, M-Fab pre-treated PELLET is at least 10-times more infectious than the corresponding SUP. Since at really high HA inactivation levels the rate of fusion-cluster formation approaches a plateau (Fig. 1b, Fig. 3), this result supports our interpretation that the PELLET advantage derives from an increase in the fusion yield. In sum, bulk endosomal fusion is unproductive and exquisitely sensitive to small perturbations in active-HA numbers. Filaments resist HA inactivation by having more opportunities for fusion-cluster formation. Very long filaments enable cell entry when active HAs become extremely rare independent of the reasons for low HA function (presence of inhibitors or near absence of activating HA cleavage); in this way, they facilitate replication allowing for mutations that can lead to adaptation.

Figure 6

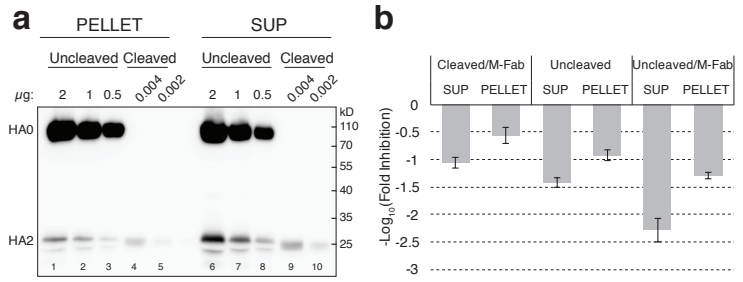

Figure 6 | Filaments resist extreme HA inactivation. a, HA2 Western blot of purified virus particles. μg refers to the total viral protein loaded. **b**, Fold reduction in recovered infectivity (plaque-forming units) per input particle (HAU) for uncleaved and/or M-Fab treated samples, relative to cleaved, untreated samples. The experiment was set up in a way to ensure that any differences among samples result from initial infections (see Methods). Data is the average and standard deviation of three independent measurements.

Conclusions

Our results define influenza filaments as viral persisters under general HA pressures. We propose a model for viral particle-size diversity serving as a phenotypic switch in the changing environment (Fig. 7). At low relative HA-directed selective pressure, majority of new infections are initiated by spherical particles; they are more numerous, use fewer resources, and are faster to internalize and assemble (Fig. 7a)[6,8]. Filaments take over when HA function is limiting and permit low level of replication (Fig. 7b). If pressure is removed, the same viral population can expand. Under sustained pressure, viral replication initiated by filaments can lead to (genetic) adaptation. For example, filaments might enable low level of replication under immune pressure, and even permit inefficiencies in HA function for immune evasion mutants, which can then be repaired by mutation. Similarly, early zoonotic transgressors in humans might be permitted by the filamentous virus population, then improved by mutation.

Targeting filamentous influenza particles should extend the effectiveness of vaccinations or fusion inhibitors, as well as help curb viral pandemics arising from adaptation of new influenza strains. One way to achieve that is to target the molecular pathways that enable filament assembly. For example, NA inhibitors disproportionately affect the release of filaments because of the higher relative NA-content on spherical particles[6]. Combining HA and NA inhibitors might thus delay resistance in an unanticipated way because NA pressure increases the proportion of spherical particles, ready targets for HA inhibitors. An attractive target for delaying resistance to HA pressures might also lie in the unique cell biology of large-cargo internalization (i.e. macropinocytosis) (Fig. 7c)[20,32-36]. Targeting cellular factors required for filamentous-virus internalization would both curb avenues for resistance by targeting host processes, and provide broad-spectrum effect against filamentous virus pathogens[1-4].

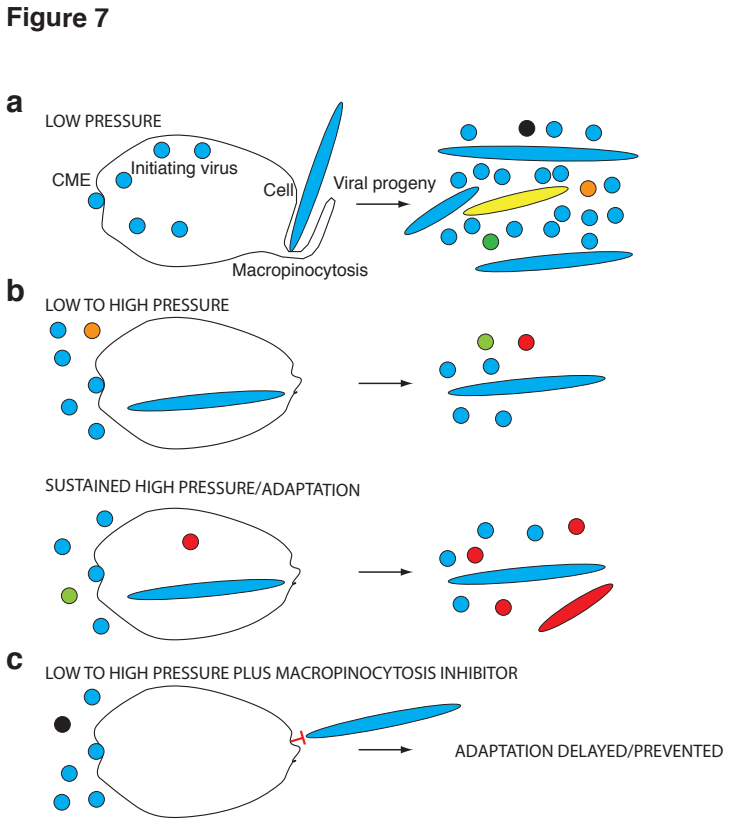

Figure 7 | A model for the influenza virus phenotypic switch. Viral progeny is pleomorphic independent of the initiating-virus morphology. Random mutations arise during replication. **a**, At low HA pressure, infections by spherical particles dominate. **b**, Filamentous particles permit cell entry and replication when spherical particles are inhibited, and can lead to adaptive mutations. **c**, Preventing macropinocytosis in combination with HA inactivation by inhibitors might avert resistance. The same strategy might apply to extending vaccine effectiveness or preventing zoonotic adaptations that can lead to pandemics. Circles, spherical particles; Ellipses, filaments; Blue, WT; Black/Orange/Green, HA mutants; Red, an adaptive HA mutant; CME, clathrin-mediated endocytosis.

SUPPLEMENTAL VIDEOS LEGENDS

Supplementary Video 1 | A sample video of the SUP hemifusion at pH 5.2 and no M-Fab. Exposure time is 0.5 sec and the video is at 80 frames per second (fps).

Supplementary Video 2 | A sample video of the PELLET hemifusion at pH 5.2 and no M-Fab. Exposure time is 0.5 sec and the video is at 80 frames per second (fps).

Supplementary Video 3 | A sample video of the SUP hemifusion at pH 5.2 and 134 nM M-Fab. Exposure time is 0.8 sec and the video is at 50 frames per second (fps).

Supplementary Video 4 | A sample video of the PELLET hemifusion at pH 5.2 and 134 nM M-Fab. Exposure time is 0.8 sec and the video is at 50 frames per second (fps).

METHODS

Reagents

Cells. MDCK.2 cells (ATCC strain CCL-34) were propagated in DMEM supplemented with 10% FBS. All infections were performed in OptiMEM (ThermoFisher Scientific) with or without 1 μg/ml TPCK-trypsin (Sigma) or M-Fab. Human embryonic kidney 293F cells were a generous gift from Stephen C. Harrison, Harvard Medical School. 293F cells were maintained in FreeStyle 293 Expression Medium (ThermoFisher Scientific), and used for Fab expression.

Antibodies. Hybridomas for SiteA and A2 antibodies were a generous gift from Judith M. White, University of Virginia. Purified LC89 antibody was a generous gift from Stephen A. Wharton, MRC National Institute for Research, London, UK. SiteA antibody binds an epitope on the HA1 head accessible on both the pre- and post-fusion HA. A2 detects an epitope on the low-pH HA1, and LC89 detects the low-pH helix-to-loop transition in HA2, residues 106-112[28]; both are reactive with HA0 and either HA1 or HA2 in Western blot.

Stochastic simulations

We used our previously published simulation codes without modification[12]. Simulation were run using the following input parameters: 1) $k_e = 0.003\text{sec}^{-1}$, where k_e is the rate of fusion peptide release, 2) $f_{un} = 0.5$, where f_{un} is the unproductive HA fraction, 3) $N_h = 3$, where N_h is the number of HA neighbors in the fusion cluster, 3) $f_{in} = 0$ to 0.97, where f_{in} is the inactive HA fraction in 0.02-0.1-value increments, and 4) input values for patch size of 50, 100, 200, 500, 1000, 3000, or 30000, to obtain actual patch sizes of 55, 121, 235, 583, 1159, 3463, or 34627, respectively. The shape of the contact patch in the simulation was kept as a circle because both unproductive and inactive HAs subdivide the area into small segments rendering the overall starting shape irrelevant for the measured outcomes.

Viruses

Viruses have A/Aichi/68 (X31) HA and the remainder of the segments from A/Udorn/72[37]. $D112_2A$ mutant was characterized previously[11]. $H17_1Y$ mutant was made and grown according to our $D112_2A$ protocol[11], except that it was passaged at a higher multiplicity of infection (MOI) of 0.1 before the final, MOI 12 infection that was not modified. Uncleaved virus was generated as described for the cleaved virus[37] except that trypsin was omitted in the final, MOI 12 infection before purification. Purifications of the short WT, $D112_2A$, and $H17_1Y$ viruses used in Fig. 5a-c were done according to our previous short-particle purification protocol on 20-60% sucrose gradient[37]. For the pelleting protocol, viruses were passed through a 30% sucrose cushion as before[37], and then subjected to 8 cycles of centrifugation at 3250 rcf for 1.5 hrs at 4 °C. For each spin, virus was diluted to 900 μl HNE20 (20 mM HEPES NaOH pH 7.4, 150 mM NaCl and 0.2 mM EDTA). After each spin, 850 μl of the supernatant volume was removed, and the pellet was resuspended in HNE20 over 6-14 hours at 4 °C. The final, 8th-spin pellet constitutes PELLET. Supernatants were combined and concentrated by a 1-hr spin at 100,000 xg (SUP).

All viruses were stored in HNE20. All purified viruses were sequenced to confirm HA-segment correctness. Completeness or near-absence of HA cleavage/activation on the purified cleaved or uncleaved virus preps was verified by A2-antibody Western blots[12]. Each virus passage

and each virus manipulation (e.g. fluorescent labeling, pelleting fractionation) were followed by measurements of specific virus infectivity using a combination of the standard plaque and hemagglutination (HA) assays to ensure a constant ratio of plaque forming units (PFU) to HA units (HAU reports on the physical virus-particle count independently of the particle morphology – see under Electron microscopy). A typical PFU/HAU ratio for the viruses is ~1-5E4. Total protein concentration of the purified virus preps was determined by the Bradford assay (BioRad).

Electron microscopy

PELLET fractions were adjusted to 2e4 HAU/ml, and SUPs and short gradient-purified fractions were adjusted to 1e5 HAU/ml. As a precaution, viruses were pretreated with 25 μM rimantadine (M2 inhibitor, Sigma) for 30 minutes at room temperature (RT) to prevent fragmentation of the filamentous particles[20]. 2% phosphotungstic-acid staining was performed as previously described[37]. Images were taken on Philips Morgagni Version3.0 TEM (80 kV, 1k CCD) using AMT Camera Version 600.335o software. Particle-size measurements were performed using custom MATLAB codes as previously described[37].

To test whether HA-assay measurements accurately report on virus-particle counts for the PELLET and SUP fractions, we performed EM-based particle counting as follows. PELLET and SUP fractions diluted as above were each mixed with a fixed concentration of purified reovirus particles. Reovirus particles have regular icosahedral structures ~85-nm in diameter[38], and appear as distinct, regular, darker objects, clearly distinguishable from influenza virus particles in the negative-stain electron micrographs. 1000-3000 total particles were counted to determine the SUP/reo and PELLET/reo particle ratios. The resultant value for PELLET/SUP particle ratio closely matched (within 30%) the PELLET/SUP particle ratio derived from their respective input HAU/ml. We therefore used HA-assay values to represent a measure of input physical particles in experiments independent of the particle morphology.

M-Fab expression, purification and labeling

The expression vectors (modified pVRC8400) for MEDI8852 Fab light and heavy chains were a generous gift from Stephen C. Harrison, Harvard Medical School. The heavy-chain construct contains the C-terminal 6xHis tag. For the fluorescent labeling of M-Fab, we modified the heavy-chain construct to also include a Sortase recognition motif LPETGG between the heavy-chain sequences and the 6xHis tag. Fab fragments were produced by transient transfection of 293F cells with polyethylenimine (PEI) (1 ug DNA: 1.5 ug PEI: 1E6 cells). Fabs were purified from the culture supernatants 5 days post transfection by a passage over a HisTrapFF column (GE Healthcare) followed by gel filtration chromatography on Superdex 200 Increase (GE Healthcare) in PBS.

A 10-fold molar excess of GGGK peptide (GenScript) was labeled with JF549-NHS-ester dye (Tocris Bioscience) in 100 mM sodium bicarbonate (pH 8.4) buffer. The desired peptide, singly labeled at the lysine residue was purified by reverse-phase HPLC on a C18 column (Grace) and its identity was confirmed by LC/MS and by its reactivity with LPETGG-M-Fab in the Sortase-labeling reaction. 6xHis-tagged SortaseA5 was expressed in *E.coli* BL21(DE3) cells and purified as previously described[39]. A 1: 1: 25 molar ratio of SortaseA5: LPETGG-M-Fab: GGGK-

JF549 was used for the Sortase-labeling reaction in PBS supplemented with 5 mM $CaCl_2$ and 5 mM $MgCl_2$ for 30 minutes at RT. Unreacted LPETGG-M-Fab and Sortase still retaining the 6xHis tag were removed from the labeled product using NiNTA resin in PBS containing 10-30 mM imidazole buffer. M-Fab-JF549 product was buffer exchanged into PBS.

Single-particle experiments

Hemifusion. We used the protocol for influenza membrane fusion described previously[11] with modifications. Virions were labeled in 25-µl reactions at 0.24 mg/mL with 1,1'-Dioctadecyl-3,3,3',3'-Tetramethylindodicarbocyanine, 4-Chlorobenzenesulfonate Salt (DiD, ThermoFisher Scientific) at 10 µM for 1.5 hours at RT. Labeled virions were used within one week. Liposomes used for planar bilayer generation consisted of 4:4:2:0.1:2 × 10^{-4} ratio of 1, 2, dioleoyl-sn-glycero-3-phosphocholine (DOPC) (Avanti Polar Lipids), 1-oleoyl-2-palmitoyl-sn-glycero-3-phosphocholine (POPC; Avanti Polar Lipids), sn-(1-oleoyl-2-hydroxy)-glycerol-3-phospho-sn-3'-(1'-oleoyl-2'-hydroxy)-glycerol (ammonium salt) (18:1 BMP (R,R)) (Avanti Polar Lipids), bovine brain disialoganglioside GD1a (Sigma), and N-((6-(biotinoyl)amino)hexanoyl)-1,2-dihexadecanoyl-sn-glycero-3-phosphoethanolamine (biotin-X DHPE) (Molecular Probes, Life Technologies), where sialic acid residues on GD1a served as receptors for influenza virions. Briefly, as before[11], planar bilayers were generated from 200-nm liposomes by vesicle-spreading method within the channels of a PDMS flow cell. They were labeled with fluorescein-conjugated streptavidin (30ug/ml, Invitrogen) that served as an external pH-probe. DiD-labeled virions (untreated or treated with M-Fab for 20 min at RT) were attached for 5-15 min. Unattached virions were washed with HNE20, and the pH was dropped with pH-4.8 or pH-5.2 buffers (10 mM citrate, 140 mM NaCl and 0.1 mM EDTA). For M-Fab-treated samples, M-Fab was included in the low pH buffer, and after 3 min of the low-pH buffer flow at 60 µl/min, the flow was reduced to 6 µl/min to preserve M-Fab. We followed hemifusion as a spike in individual virion fluorescence resulting from DiD-fluorescence dequenching upon dilution in the target membrane. All experiments were performed at 23±0.4 °C.

Fluorescent M-Fab binding. Cleaned and plasma etched slides[11] were silanized with N-(2-aminoethyl)-3-aminopropyltrimethoxysilane, amino silane (United Chemical Technologies) and then PEGylated with a mixture of biotin-PEG-SVA-5000 and mPEG-SVA-5000 (1:40 molar ratio; Laysan, Inc.) according to a published protocol[40]. They were dried and stored protected from light and moisture at -80 °C until use. For fluorescent M-Fab binding experiments, PDMS flow cells were assembled as before[11] and the following sequence of steps was followed each time: 1) PBS wash, 5 min at 30 µl/min; 2) 5-min incubation with 0.2 mg/ml NeutrAvidin (ThermoFisher Scientific); 3) PBS wash, 2 min at 30 µl/min; 4) 6-min incubation with biotinylated SiteA antibody (0.1 mg/ml); 5) PBS then HNE washes, 2 min at 30 µl/min each; 6) imaging for background subtraction; 7) 7-min incubation with unlabeled virions pre-incubated with M-Fab-JF549 for 20 min at RT; 8) HNE20 wash, 30 sec at 30 µl/min; 9) imaging for intensity measurements, pH7.4 (4 fields of view); 10) pH-4.8 buffer wash, 3-min at 60 µl/min, and incubation for the total of 20 min; 11) imaging for intensity measurements, pH4.8 (4 fields of view, including one shared with pH7.4-imaging). When SiteA antibody was replaced by a non-specific mouse antibody, a very small amount of nonspecific sticking of influenza virus particles was observed (~1%).

Microscope configuration. The excitation pathway was unchanged relative to our previous setup[11], except that we now added a 647-nm laser (Obis, Coherent) and the diameter of the illuminated area was approximately 136 μm. Total internal reflection (TIR) illumination was achieved using a commercial micro-mirror platform, RM21 (Mad City Labs, Inc.) essentially as described[41]. Briefly, the system spatially separates the excitation and emission light within the objective lens and eliminates the need for a dichroic. An integrated XY micro-positioning, and XYZ nano-positioning stage is designed around a fixed objective lens (Olympus 60X ApoN NA=1.49) with the open access to its back aperture required for micro-mirror-based illumination. The system was additionally equipped with a 180-mm achromatic tube-lens. Image was projected onto an entire 512 x 512 pixel EM-CCD sensor (Model C9100-13; Hamamatsu) for the final pixel representation of 160 nm.

For the single-particle hemifusion experiments, 488-nm laser (Obis, Coherent) was used to excite fluorescein, and 647-nm laser (Obis, Coherent) was used to simultaneously excite DiD. The power of the 488-nm laser was 1-2 μW, and the 647 laser was 0.25-1 μW over the illuminated area. Exposure time was between 0.4 and 0.8 sec, depending on the virus and the inhibitor concentration. For the fluorescent intensity measurements of M-Fab-JF549 binding to virus particles, the power of the 552-nm laser was 5.1 μW over the illuminated area, and the exposure time was 1 sec.

Data analysis

All data analysis was done in MATLAB (MathWorks).

Single-particle hemifusion. Particle centroids, pH-drop time, and DiD-dequenching times for individual particles were extracted from time-lapse movies as described[30]. We defined hemifusion yield as the percent of detected particles that hemifused within 20 minutes of pH drop. Probability-density distributions of hemifusion lag times were fitted with gamma distribution to derive mean lag-times[12,29,30,37].

Derivation of long-particle hemifusion kinetics. Hemifusion-yield curves for PELLET and SUP particles (Fig. 3b) were scaled to adjust the no-M-Fab hemifusion to 100%. We justify this in the context of our previous analysis, which found that the lower than 100% yield in the absence of HA inhibition reports on the efficiency of the assay, but the probability of fusion-cluster formation is 100%[12]. This assumption is further justified by PELLET maintaining unreduced hemifusion yield at 67 nM M-Fab (Fig. 3b); if fusion-cluster formation was already limiting for no M-Fab, HA inactivation would cause a further reduction in hemifusion yield (Fig. 1b)[12]. In what follows, we illustrate with one example how the scaled yield-data were then processed to derive long-particle yields. At 268 nM M-Fab, there is 80% (Fig. 3c) and 70% (not shown, scaled data from Fig. 3b) reduction in hemifusion yield for SUP and PELLET, respectively. Since SUP-like particles represent approximately 50% of the PELLET (Table 1), the loss of fusing particles determined for the SUP can account for 40% loss in the PELLET; the remaining 30% must have resulted from inhibition of long particles, and the long-particle yield is thus 70% (Fig. 3c). For samples where PELLET yield-reduction was not greater than that predicted from the SUP data, long-particle yield was set to 100%.

We performed bi-gamma fitting of the PELLET lag-time distributions (Fig. 3a, *bottom*) using the following formula,

$$p(t) = f_1 \underbrace{\frac{k_1^{N_1} t^{N_1-1}}{\Gamma(N_1)} e^{-k_1 t}}_{p_{\mathrm{Gamma}}(t;N1,k1)} + (1-f_1) \underbrace{\frac{k_2^{N_2} t^{N_2-1}}{\Gamma(N_2)}}_{p_{\mathrm{Gamma}}(t;N2,k2)}$$

Here, p_{Gamma}(t; N, *k*) is the probability density function of the Gamma distribution with rate *k* and shape parameter N, and *f*1 is the fraction of population whose distribution is represented by (N1, *k*1) or the SUP-like particles, with the remainder sampling a (N2, *k*2) or the long-particle distribution. *f*1, *k*1, and N1 values were fixed, and N2, and *k*2 were derived from the fits. To fix values, *k*1 and N1 were derived from single-gamma fitting of the SUP data (Fig. 3a, *top/red lines*). *f*1 was calculated as follows. From the SUP- and long-particle yield values (Y_{SUP} and Y_{PELLET}) (Fig. 3c), we calculated the fraction of the observed hemifusion events contributed by the long particles in the PELLET, $f_{long} = Y_{long} / (Y_{long} * 0.5 + Y_{SUP} * 0.5)$. The two yield values were multiplied by 0.5 because SUP-like particles represent approximately 50% of the PELLET (Table 1). *f*1 was fixed at (1- f_{long}). We show the bi-gamma fit curves (black lines), and the underlying curves for long (blue lines) and SUP-like particles (red lines) in the PELLET (Fig. 3a, *bottom*).

Particle fluorescence-intensity measurements. The intensity analysis consists of three codes. The first code averages the first 10 frames of the particle movies (M-Fab-JF549 particles) and the no-particle movie (background), and subtracts the background image from the averaged particle images. The second code plots the background-processed image and prompts the user to manually draw regions of interest (masks) around particles whose intensity is to be quantified. Manual masks were preferred in this case because of the long particles that can be mistaken for multiple particles by automated particle-detection codes. The third code then integrates intensities within the masks.

Infectivity measurements

scTCID50. Virus was pre-incubated with or without M-Fab in OptiMEM for 30 minutes at RT, then serially diluted 4-fold in the same media. Trypsin was omitted to prevent activation of the released virus and new rounds of infection. Confluent monolayers of MDCK.2 cells in 96-well plates were washed with HBSS twice, and 100 µl of the virus dilutions were added to wells. The highest input virus concentration was 2-7*10^3 HAU/ml. Cells were fixed 24 hrs post infection with 3.7% formaldehyde, then stained with crystal violet. Plates were scanned using Gel Doc (Biorad), and the extent of cell death in each well evaluated by densitometry using ImageJ. The densitometry value in wells with complete cell death (background) was subtracted from all measurements, and the amount of cell death quantified relative to wells with no cell death. $scTCID_{50}$ titer is derived from the resultant plots of cell death versus particle concentration as the inverse of the particle concentration that resulted in 50% cell death. Relative reduction in infectivity was quantified as the ratio of $scTCID_{50}$ values for the untreated (baseline) and M-Fab-treated samples. We obtained the same baseline titers (tested with WT and $H17_1Y$ PELLET and SUP) when new rounds of infection were additionally prevented by the addition of 20 mM ammonium chloride[42] 4-hours post infection, confirming that our experimental setup resulted in a single-cycle of infection. For

each experiment, each condition was done in duplicate. At least three independent experiments were performed. The same results were obtained with a second clone of each WT and mutant viruses.

Modified plaque assay. Uncleaved PELLET and SUP viruses were diluted to 500 HAU/ml (for the uncleaved/M-Fab treated samples) or 50 HAU/ml (for the remaining samples) in OptiMEM for pre-treatment. To obtain cleaved samples, uncleaved viruses were pre-treated with 1 μg/ml TPCK-trypsin (Sigma) for 1 hr at RT, and trypsin was inactivated with 20 μg/ml soybean trypsin inhibitor (Sigma). For M-Fab pre-treatment, precleaved or uncleaved viruses were incubated with 268 nM M-Fab for 30 min at RT. The pre-treatment reactions were directly used as the first virus dilution in the subsequent plaque assay, and were serially diluted 10-fold in OptiMEM (no additives) for 5 more steps. 100 μl of the virus dilutions were attached to confluent monolayers of MDCK.2 cells in 6-well plates for 1 hour at RT. Unattached virus and free M-Fab were washed twice with HBSS, and viruses were allowed to internalize for 4 hours at 37 °C in OptiMEM (no additives). Media was then replaced with OptiMEM/0.6% Oxoid Agar/1 μg/ml TPCK-trypsin, and the plates were incubated for 2.5 more days at 34 °C for plaque formation. Removal of M-Fab after pre-incubation and virus attachment, and addition of trypsin only after virus internalization, ensure that any differences among samples are due to differences in the initial infection by SUP and PELLET. An additional control had trypsin present in all virus dilutions and during the 4-hour internalization phase. No infectivity difference was detected between this sample and the cleaved sample where trypsin was inactivated after digestion, confirming complete virus activation by the 1-hour trypsin treatment. The cleaved-virus reference in the Western blot (Fig. 6a) was a fully cleaved virus prepared in a standard way (not deriving from the uncleaved virus prep). The Western blot used LC89 antibody for HA0 and HA2 detection.

ACKNOWLEDGMENTS

We thank Goran Bajic (Harvard Medical School) for help with Fab expression and purification, Milos Popovic (Boston University) for help with analysis codes, and Stephen C. Harrison (Harvard Medical School) and Bruce L. Goode (Brandeis University) for comments on the manuscript. We acknowledge support from the NIH Director's New Innovator Award to TI, 1DP2GM128204, and the NSF MRSEC DMR-1420382.

AUTHOR CONTRIBUTIONS

TL, Experiment design, Acquisition of data, Analysis and interpretation of data; ZL, ML, ED, Acquisition of data, Analysis and interpretation of data; TI, Conception and design, Experiment design, Acquisition of data, Analysis and interpretation of data, Writing of the manuscript.

REFERENCES

1 Battisti, A. J. *et al.* Structure and assembly of a paramyxovirus matrix protein. *Proc Natl Acad Sci U S A* **109**, 13996-14000, doi:10.1073/pnas.1210275109 (2012).

2 Bharat, T. A. *et al.* Structural dissection of Ebola virus and its assembly determinants using cryo-electron tomography. *Proc Natl Acad Sci U S A* **109**, 4275-4280, doi:10.1073/pnas.1120453109 (2012).

3 Hyatt, A. D., Zaki, S. R., Goldsmith, C. S., Wise, T. G. & Hengstberger, S. G. Ultrastructure of Hendra virus and Nipah virus within cultured cells and host animals. *Microbes Infect* **3**, 297-306 (2001).

4 Liljeroos, L., Krzyzaniak, M. A., Helenius, A. & Butcher, S. J. Architecture of respiratory syncytial virus revealed by electron cryotomography. *Proc Natl Acad Sci U S A* **110**, 11133-11138, doi:10.1073/pnas.1309070110 (2013).

5 Chu, C. M., Dawson, I. M. & Elford, W. J. Filamentous forms associated with newly isolated influenza virus. *Lancet* **1**, 602, doi:10.1016/s0140-6736(49)91699-2 (1949).

6 Vahey, M. D. & Fletcher, D. A. Low-Fidelity Assembly of Influenza A Virus Promotes Escape from Host Cells. *Cell* **176**, 678, doi:10.1016/j.cell.2019.01.009 (2019).

7 Roberts, P. C., Lamb, R. A. & Compans, R. W. The M1 and M2 proteins of influenza A virus are important determinants in filamentous particle formation. *Virology* **240**, 127-137, doi:10.1006/viro.1997.8916 (1998).

8 Dadonaite, B., Vijayakrishnan, S., Fodor, E., Bhella, D. & Hutchinson, E. C. Filamentous influenza viruses. *J Gen Virol* **97**, 1755-1764, doi:10.1099/jgv.0.000535 (2016).

9 Calder, L. J., Wasilewski, S., Berriman, J. A. & Rosenthal, P. B. Structural organization of a filamentous influenza A virus. *Proc Natl Acad Sci U S A* **107**, 10685-10690, doi:10.1073/pnas.1002123107 (2010).

10 Wasilewski, S., Calder, L. J., Grant, T. & Rosenthal, P. B. Distribution of surface glycoproteins on influenza A virus determined by electron cryotomography. *Vaccine* **30**, 7368-7373, doi:10.1016/j.vaccine.2012.09.082 (2012).

11 Ivanovic, T., Choi, J. L., Whelan, S. P., van Oijen, A. M. & Harrison, S. C. Influenza-virus membrane fusion by cooperative fold-back of stochastically induced hemagglutinin intermediates. *Elife* **2**, e00333, doi:10.7554/eLife.00333 (2013).

12 Ivanovic, T. & Harrison, S. C. Distinct functional determinants of influenza hemagglutinin-mediated membrane fusion. *Elife* **4**, e11009, doi:10.7554/eLife.11009 (2015).

13 Calder, L. J. & Rosenthal, P. B. Cryomicroscopy provides structural snapshots of influenza virus membrane fusion. *Nat Struct Mol Biol* **23**, 853-858, doi:10.1038/nsmb.3271 (2016).

14 Kallewaard, N. L. *et al.* Structure and Function Analysis of an Antibody Recognizing All Influenza A Subtypes. *Cell* **166**, 596-608, doi:10.1016/j.cell.2016.05.073 (2016).

15 Bradford, M. J., Guerette, P. A. & Roff, D. A. Testing hypotheses of adaptive variation in cricket ovipositor lengths. *Oecologia* **93**, 263-267, doi:10.1007/BF00317680 (1993).

16 Balaban, N. Q., Merrin, J., Chait, R., Kowalik, L. & Leibler, S. Bacterial persistence as a phenotypic switch. *Science* **305**, 1622-1625, doi:10.1126/science.1099390 (2004).

17 Rego, E. H., Audette, R. E. & Rubin, E. J. Deletion of a mycobacterial divisome factor collapses single-cell phenotypic heterogeneity. *Nature* **546**, 153-157, doi:10.1038/nature22361 (2017).

18 Choppin, P. W., Murphy, J. S. & Tamm, I. Studies of two kinds of virus particles which comprise influenza A2 virus strains. III. Morphological characteristics: independence to morphological and functional traits. *J Exp Med* **112**, 945-952, doi:10.1084/jem.112.5.945 (1960).

19 Seladi-Schulman, J., Steel, J. & Lowen, A. C. Spherical influenza viruses have a fitness advantage in embryonated eggs, while filament-producing strains are selected in vivo. *J Virol* **87**, 13343-13353, doi:10.1128/JVI.02004-13 (2013).

20 Rossman, J. S., Leser, G. P. & Lamb, R. A. Filamentous influenza virus enters cells via macropinocytosis. *J Virol* **86**, 10950-10960, doi:10.1128/JVI.05992-11 (2012).

21 Noda, T. *et al.* Architecture of ribonucleoprotein complexes in influenza A virus particles. *Nature* **439**, 490-492, doi:10.1038/nature04378 (2006).

22 Russell, C. A. *et al.* The global circulation of seasonal influenza A (H3N2) viruses. *Science* **320**, 340-346, doi:10.1126/science.1154137 (2008).

23 Mair, C. M., Ludwig, K., Herrmann, A. & Sieben, C. Receptor binding and pH stability - how influenza A virus hemagglutinin affects host-specific virus infection. *Biochim Biophys Acta* **1838**, 1153-1168, doi:10.1016/j.bbamem.2013.10.004 (2014).

24 Chen, J. *et al.* Structure of the hemagglutinin precursor cleavage site, a determinant of influenza pathogenicity and the origin of the labile conformation. *Cell* **95**, 409-417, doi:10.1016/s0092-8674(00)81771-7 (1998).

25 Wilson, I. A., Skehel, J. J. & Wiley, D. C. Structure of the haemagglutinin membrane glycoprotein of influenza virus at 3 A resolution. *Nature* **289**, 366-373, doi:10.1038/289366a0 (1981).

26 Xiong, X. *et al.* Receptor binding by a ferret-transmissible H5 avian influenza virus. *Nature* **497**, 392-396, doi:10.1038/nature12144 (2013).

27 Bullough, P. A., Hughson, F. M., Skehel, J. J. & Wiley, D. C. Structure of influenza haemagglutinin at the pH of membrane fusion. *Nature* **371**, 37-43, doi:10.1038/371037a0 (1994).

28 Wharton, S. A. *et al.* Electron microscopy of antibody complexes of influenza virus haemagglutinin in the fusion pH conformation. *EMBO J* **14**, 240-246 (1995).

29 Otterstrom, J. J. *et al.* Relating influenza virus membrane fusion kinetics to stoichiometry of neutralizing antibodies at the single-particle level. *Proc Natl Acad Sci U S A* **111**, E5143-5148, doi:10.1073/pnas.1411755111 (2014).

30 Floyd, D. L., Ragains, J. R., Skehel, J. J., Harrison, S. C. & van Oijen, A. M. Single-particle kinetics of influenza virus membrane fusion. *Proc Natl Acad Sci U S A* **105**, 15382-15387, doi:10.1073/pnas.0807771105 (2008).

31 Thoennes, S. *et al.* Analysis of residues near the fusion peptide in the influenza hemagglutinin structure for roles in triggering membrane fusion. *Virology* **370**, 403-414, doi:10.1016/j.virol.2007.08.035 (2008).

32 de Vries, E. *et al.* Dissection of the influenza A virus endocytic routes reveals macropinocytosis as an alternative entry pathway. *PLoS Pathog* **7**, e1001329, doi:10.1371/journal.ppat.1001329 (2011).

33 Nanbo, A. *et al.* Ebolavirus is internalized into host cells via macropinocytosis in a viral glycoprotein-dependent manner. *PLoS Pathog* **6**, e1001121, doi:10.1371/journal.ppat.1001121 (2010).

34 Saeed, M. F., Kolokoltsov, A. A., Albrecht, T. & Davey, R. A. Cellular entry of ebola virus involves uptake by a macropinocytosis-like mechanism and subsequent trafficking through early and late endosomes. *PLoS Pathog* **6**, e1001110, doi:10.1371/journal.ppat.1001110 (2010).

35 Krzyzaniak, M. A., Zumstein, M. T., Gerez, J. A., Picotti, P. & Helenius, A. Host cell entry of respiratory syncytial virus involves macropinocytosis followed by proteolytic activation of the F protein. *PLoS Pathog* **9**, e1003309, doi:10.1371/journal.ppat.1003309 (2013).

36 Pernet, O., Pohl, C., Ainouze, M., Kweder, H. & Buckland, R. Nipah virus entry can occur by macropinocytosis. *Virology* **395**, 298-311, doi:10.1016/j.virol.2009.09.016 (2009).

37 Ivanovic, T. *et al.* Kinetics of proton transport into influenza virions by the viral M2 channel. *PLoS One* **7**, e31566, doi:10.1371/journal.pone.0031566 (2012).

38 Zhang, X. *et al.* Features of reovirus outer capsid protein mu1 revealed by electron cryomicroscopy and image reconstruction of the virion at 7.0 Angstrom resolution. *Structure* **13**, 1545-1557, doi:10.1016/j.str.2005.07.012 (2005).

39 Chen, I., Dorr, B. M. & Liu, D. R. A general strategy for the evolution of bond-forming enzymes using yeast display. *Proc Natl Acad Sci U S A* **108**, 11399-11404, doi:10.1073/pnas.1101046108 (2011).

40 Diao, J. *et al.* A single vesicle-vesicle fusion assay for in vitro studies of SNAREs and accessory proteins. *Nat Protoc* **7**, 921-934, doi:10.1038/nprot.2012.020 (2012).

41 Larson, J. *et al.* Design and construction of a multiwavelength, micromirror total internal reflectance fluorescence microscope. *Nat Protoc* **9**, 2317-2328, doi:10.1038/nprot.2014.155 (2014).

42 Daniels, R. S. *et al.* Fusion mutants of the influenza virus hemagglutinin glycoprotein. *Cell* **40**, 431-439, doi:10.1016/0092-8674(85)90157-6 (1985).